JOURNAL OF PROPULSION AND POWER
Vol. 18, No. 6, November–December 2002

Modeling Cavitating Venturi Flows

Changhai Xu* and Stephen D. Heister†
Purdue University, West Lafayette, Indiana 47907
and
Robert Field‡
NASA Stennis Space Center, Mississippi 39529

Simulations of various venturi orifice cavitating flows were performed using a homogeneous flow model. The dynamics of a bubble response per the Rayleigh–Plesset equation are cast into constitutive equation for the density for the pseudofluid, and the turbulence is approximated by the $k - \omega$ turbulence model. The computed results show that cavitation develops at the throat and its downstream region grows and collapses in a quasi-periodic fashion. The size of the cavity grows as the cavitation number for the flow is reduced. The mass flow rate through the cavitating venturi oscillates periodically essentially in phase with the vapor cloud in the diffuser. Venturi flow rate, oscillation frequency, and cavitation extent are characterized for a wide range of conditions and are compared against experimental data. Results indicate that computations are accurate to within a few percent in flow rate for the venturis modeled in the project.

Nomenclature

C_d = discharge coefficient
D = throat diameter, in.
f = oscillation frequency
K = cavitation number
L_c = cavitation length
L_D = diffuser length
$\dot{m}$ = orifice mass flow rate
n = bubble number density
P = pressure
Re = Reynolds number
r = radial coordinate
t = time
$\tilde{u}$ = Favre-averaged velocity
V = velocity
z = axial coordinate
α = void fraction
μ = viscosity
ρ = fluid pseudodensity

Subscripts

c = cavitation length
D = discharge coefficient
l = liquid
v = vapor
1 = inlet
2 = outlet

Introduction

CAVITATING venturis are one of the simplest flow control devices and have broad uses over a range of industries as a result of this fact. Numerous industrial flow processes are controlled by such devices, and they are commonly used to meter propellants in liquid rocket engine tests. In this latter application the venturi serves as a flowmeter and provides a mechanism to keep flow rate constant during the firing. The constant flow feature is particularly useful during the ignition transient when the downstream pressure in the combustion chamber is rising rapidly.

A cavitating venturi typically consists of a converging section, a short straight throat section, and a diffuser as shown in Fig. 1. When the downstream pressure P_2 is less than a 85–90% of upstream pressure P_1, cavitation starts to occur at the throat, and the flow through the venturi orifice becomes "choked." Generally, it is believed that further decrease in downstream pressure will not result in any increase of the mass flow rate.

In spite of the large number of applications of this device, relatively little research has been conducted into its operating characteristics and mechanisms of operation. Early work pertaining to the rocket application[1–3] provided basic venturi sizing data and some limited experiments with Plexiglas® models to highlight the vapor location. More recently, Sun and Yang[4] studied the oscillatory behavior and erosion characteristics in a Delavale nozzle with a geometry essentially the same as those used in cavitating venturis. This group measured cavitation lengths and erosion rates for long-duration tests on an aluminum venturi. The rocket community typically does not experience measurable erosion of these devices.[2] One might attribute this conclusion to the fact that the venturis are typically made of harder materials and that test durations are relatively short.

In the mid 1990s a series of investigations were pursued in connection with venturis used on an ammonia cooling loop for the space station. Ungar et al.[5] investigated the performance of cavitating venturis under low inlet subcooling (pressure difference between the inlet pressure and the saturation pressure at the inlet temperature). They found when the downstream pressure is increased so that the venturi is operating in unchoked mode and is subsequently decreased "overflow can occur." During overflow, the flow rate exceeds the maximum choked flow rate as much as two times. The overflow condition has been found to persist with a hysteresis effect until the pressure ratio is decreased to a much lower value. Physically, this behavior can be attributed to hydrodynamic nonequilibrium effects that delay the onset of cavitation to pressures significantly below the equilibrium vapor pressure.

Ungar and Mal[6] also investigated alternative geometries to mitigate the overflow condition by placing an aft-facing step in the throat region. The step causes very low pressures locally, ensuring cavitation at this locale. Numerically, Navickas and Chen[7] used an axisymmetric computational fluid dynamics program to model

---

Received 14 February 2002; revision received 24 July 2002; accepted for publication 29 July 2002.

*Graduate Research Assistant, School of Aeronautics and Astronautics.

†Professor, School of Aeronautics and Astronautics, 1282 Grissom Hall.

‡Aerospace Technologist, Propulsion Test Directorate.

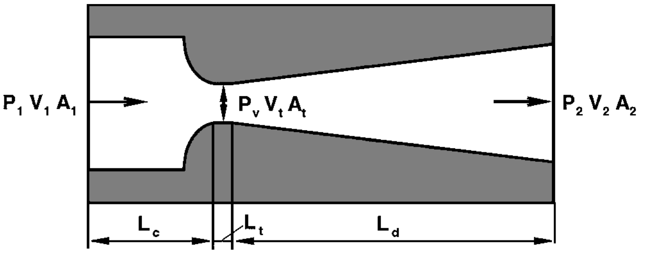

Fig. 1 Schematic of a cavitating venturi noting design conditions.

the cavitating venturi flow characteristics for the ammonia coolant loop application. However, the program they used cannot predict the onset of cavitation.

Despite these advances, there are no comprehensive works detailing the unsteady performance of these devices over a wide range of operating conditions. The recent advances in simulating two-phase flows of this type make it possible to provide multidimensional calculations of these flows. In the present work a homogeneous flow treatment is applied to treat the unsteady two-phase flowfield. Homogeneous, or pseudodensity, models assume that on the microscopic level two phases are fully mixed and homogeneous and the local density is a measure of the void fraction. This approach requires a constitutive relation for pseudodensity, a fictitious variable, in order to complete the set of governing equations.

Chen and Heister[8] developed a constitutive relation based on the dynamics of a single bubble in an unsteady environment. This treatment allows bubbles to respond not only to the local pressure field, but to account for the inertia of the fluid displaced by growth or shrink of bubbles in a time-dependent manner. The model has been used to address hydrodynamic nonequilibrium effects such as those experienced in the ammonia coolant loop. This model has been validated extensively against data pertaining to cavitating orifice flows.[9–11]

The unsteady discharge and flowfield characteristics are studied for a variety of cavitating venturis with primary motivation to study conditions pertinent to rocket testing applications. The working fluids include liquid oxygen, liquid nitrogen, liquid hydrogen, and water. The venturis studied have been tested by the groups at NASA Stennis Space Center and Pennsylvania State University, University Park, Pennsylvania. The models are briefly described in the following section. Results are presented for several cases, and conclusions are presented to complete the paper.

Modeling Description

Figure 1 provides a simple schematic highlighting various parameters and the geometry of a typical cavitating venturi. We choose the Bernoulli velocity at the throat V_t, the venturi throat diameter D, liquid density ρ_l, and dynamic viscosity μ_l as dimensions. Under this nondimensionalization two parameters emerge and characterize the flow:

$$Re = \rho_l V_t D/\mu_l, \qquad K = (P_1 - P_v)/(P_1 - P_2) \tag{1}$$

where P_1 and P_2 are inflow and outflow pressure, respectively; P_v is the vapor pressure; and V_t is the Bernoulli velocity. The Reynolds number Re measures viscous effects as in all Navier–Stokes solutions. The cavitation number K is the most important parameter in the present work as this will set the overall extent of cavitation in the device.

The Bernoulli velocity is computed assuming the static pressure of the fluid drops to vapor pressure P_v and is still not vaporized at the throat. Under this idealized condition application of the Bernoulli and continuity equations at the inlet and the throat give

$$\tfrac{1}{2}\rho_l V_1^2 + P_1 = \tfrac{1}{2}\rho_l V_t^2 + P_v \tag{2}$$

$$\rho_l V_1 A_1 = \rho_l V_t A_t \tag{3}$$

Combining Eqs. (2) and (3), we get the Bernoulli velocity at the throat:

$$V_t = \sqrt{\frac{2(P_1 - P_v)}{\rho_l}\frac{1}{1 - (A_t/A_1)^2}} \tag{4}$$

The development of the homogeneous fluid model is discussed in detail in prior works,[8–11] and so only a brief description is provided herein. The model is essentially a Navier–Stokes solution for a variable density flow in that the pseudodensity is the ficticious parameter introduced to reflect the local void fraction in the flow. The viscosity of the mixture is frequently written as a void fraction weighted average under this architecture.[12] In the case where the liquid viscosity is much greater than that of the gas, this result reduces to the liquid viscosity weighted with the local liquid fraction [$\mu = (1 - \alpha)\mu_l$; the local volume fraction of vapor in the two-phase mixture]. In this case the result reduces to

$$\mu = \rho\mu_l \tag{5}$$

where $\rho = 1 - \alpha$, assuming the mass of the gas phase is negligible in comparison to the liquid. This approach has provided good agreement with experimental results in orifices and slots and for the extent of cavitation on hydrodynamic headforms.[8–10]

The homogeneous two-phase treatment requires an additional relation for pseudodensity to close the problem. We have been able to derive an applicable form of the Rayleigh–Plesset equation[8] of bubble dynamics under the assumption of negligible fission/fusion events, slip between phases, and surface tension forces. Although such events/forces are clearly present in the real flow, the simplified result does properly reflect the growth/collapse of an average-sized bubble as a result of the transient pressure field and inertial forces on its periphery. The resultant expression becomes[8]

$$\frac{D^2\rho}{Dt^2} = \frac{6\alpha'(1+\alpha'+\alpha'^2)^2}{L_0^2(2+\alpha')(1-\alpha'^3)^{\frac{1}{3}}}(P - P_v) + \left[\frac{11\alpha'^3 - \alpha'^2 - \alpha' - 1}{6\alpha'^3(1-\alpha'^3)} - \frac{1+4\alpha'+\alpha'^2}{6\alpha'^2(2+\alpha')(1+\alpha'+\alpha'^2)}\right]\left(\frac{D\rho}{Dt}\right)^2 \tag{6}$$

Here, $\alpha' = \sqrt[3]{(1-\rho)}$, P is the local pressure, and P_v is the vapor pressure. The quantity L_0 is a characteristic length scale, which is a function of the site density:

$$L_0^2 = (3/4\pi n_o)^{\frac{2}{3}} \tag{7}$$

Here, n_o is the nondimensional site density. Letting the dimensional site density, the number of cavitation sites per unit volume, be represented by $\hat{n}_o$, then

$$n_o = \hat{n}_o\hat{D}^3 \tag{8}$$

where $\hat{D}$ is a characteristic length used in the nondimensionalization of the governing equations.

Equation (6) is integrated in time to account for the spatially and temporally varying pressure field [first term on right-hand-side of Eq. (6)] and inertial forces ($D\rho/Dt$ term) on the growth/collapse of the bubbles. The relation does account for hydrodynamic nonequilibrium effects in that the inertia term does become important at very small length scales (where L_0 becomes very large). Scaling effects have been addressed successfully using the model.[8] In the cavitation site density $\hat{n}$ is the lone parameter introduced by this treatment, and its influence will be addressed in the Results discussion.

We assume the flow inside a venturi is axisymmetric. Therefore, under the homogeneous flow treatment, the governing equations take the following forms:

$$\frac{\partial(r\bar{\rho})}{\partial t} + \frac{\partial(r\bar{\rho}\tilde{u}_i)}{\partial x_i} = 0 \tag{9}$$

$$\frac{\partial(r\bar{\rho}\tilde{u}_i)}{\partial t} + \frac{\partial(r\bar{\rho}\tilde{u}_j\tilde{u}_i)}{\partial x_j} = -r\frac{\partial P}{\partial x_i} + r\frac{\partial}{\partial x_j}[\bar{t}_{ji} + \tau_{ji}] \tag{10}$$

where, P and $\bar{\rho}$ are time-averaged pressure and density, respectively, and $\bar{t}_{ij}$ and τ_{ij} are the viscous stress tensor and mass-averaged Reynolds-stress tensor, respectively.

The $k - \omega$ model[13] takes the following form:

$$\frac{\partial(r\bar{\rho}k)}{\partial t} + \frac{\partial(r\bar{\rho}\tilde{u}_j k)}{\partial x_j} = r\tau_{ij}\frac{\partial \tilde{u}_i}{\partial x_j} - rRe\beta^*\bar{\rho}k\omega + \frac{\partial}{\partial x_j}\left[\frac{r}{Re}(\mu + \sigma^*\mu_T)\frac{\partial k}{\partial x_j}\right] \tag{11}$$

$$\frac{\partial(r\bar{\rho}\omega)}{\partial t} + \frac{\partial(r\bar{\rho}\tilde{u}_j \omega)}{\partial x_j} = r\alpha\frac{\omega}{k}\tau_{ij}\frac{\partial \tilde{u}_i}{\partial x_j} - rRe\beta\bar{\rho}\omega^2 + \frac{\partial}{\partial x_j}\left[\frac{r}{Re}(\mu + \sigma\mu_T)\frac{\partial \omega}{\partial x_j}\right] \tag{12}$$

Here, we used the same treatment for the eddy viscosity μ_T as that for the dynamic viscosity μ for two-phase mixture

$$\mu_T \propto (1-\alpha)(k/\omega) = \bar{\rho}(k/\omega) \tag{13}$$

where $\bar{\rho} = 1 - \alpha$ as outlined before. The implication of Eq. (13) is that the contribution of gas phase to turbulence is neglected compared to that of liquid phase because $\rho_g \ll \rho_l$. Including the closure coefficient, eddy viscosity is evaluated by

$$\mu_T = \alpha^*\bar{\rho}(k/\omega) \tag{14}$$

The closure coefficients and auxiliary relations of the $k - \omega$ model are given in Ref. 13. A detailed account of the turbulence treatment is provided in Ref. 14.

Numerics

The governing equations are solved using the Marker and Cell method with a staggered mesh. Figure 2 shows the locations of all flow variables. The base nodes of scalar variables (P, ρ, k, ω) and the base nodes of velocity vectors are allocated in an alternate manner in space. The Poisson equation of pressure at an interior control volume involves the pressure variables at the base node and all of its eight neighbors. Therefore, this scheme results in a nondiagonal system for pressure, with a similar matrix structure for the turbulent quantities k and ω. The system equations are solved by the successive line overrelaxation method. The mean-flow equations and the turbulence transport equations are solved sequentially. For the detailed solution procedure of the coupling of the constitutive pseudodensity relation and the Navier–Stokes equation, see Ref. 8.

Figure 3 shows a portion of a typical computational mesh and the boundary conditions employed. The complete mesh is significantly larger than that portion shown and extends a total of 10 throat radii upstream of the entry to the convergent section and 24 radii downstream of the diffuser exit. Numerical studies indicate that solutions are insensitive to the location of the inlet and outlet boundaries when placed as noted. On the wall no-slip conditions were applied. On the symmetry plane standard symmetry conditions were used. On the outflow boundary constant pressure (P_2) is specified, and first-order of extrapolation is used for velocity and turbulence parameters k and ω. The pressure and velocity at the inflow boundary are treated in a similar fashion such that the mass flow is computed based on the imposed pressure drop through the device. The k and ω values at the inflow boundary are given by the following formulation:

$$k_{\text{in}} = 0.1\% \cdot V_t^2, \qquad \omega_{\text{in}} = \sqrt{k}\big/\lambda D \tag{15}$$

where λ is a length scale factor. In this study it was set to 500.

A grid-refinement study showed that a mesh of 150 × 70 is sufficient to resolve characteristics of interest within the flowfield. Results of this assesment are summarized in Fig. 4, which depicts the mass flow of the device for three separate meshes. The 150 × 70 grid

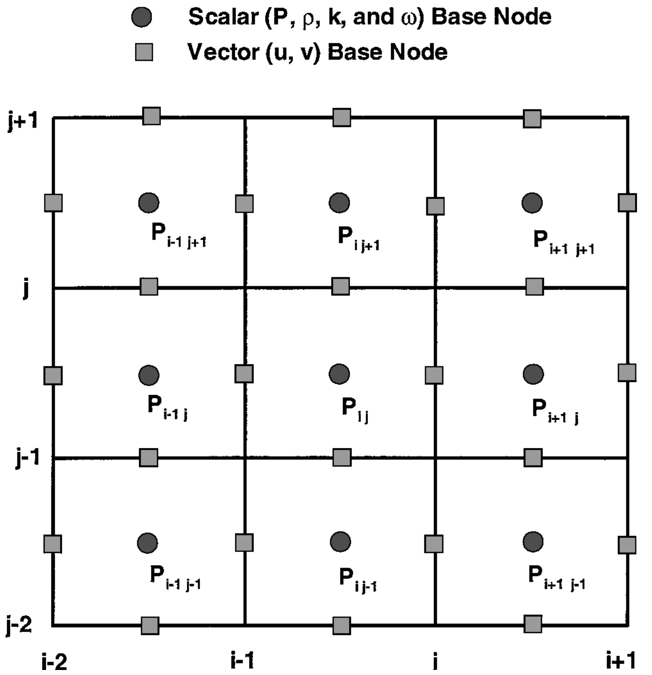

Fig. 2 Marker and Cell scheme mesh star.

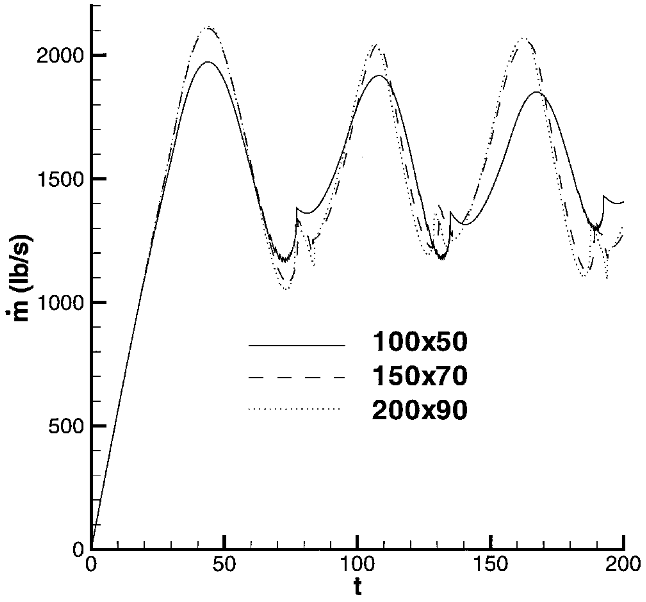

Fig. 4 Grid function convergence study showing venturi mass-flow history for a variety of different meshes using conditions noted in case 4 in Table 1. The 150 × 70 mesh was selected for use in calculations.

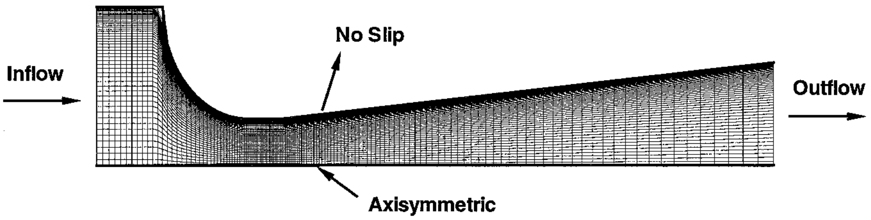

Fig. 3 Computational mesh and boundary conditions.

was deemed to be adequate to resolve the mass-flow history for the purposes of the study. The dimensionless time step used is 0.0005, and the iteration number taken to solve the system equations for pressure k and ω per time step varies periodically, from several hundreds to only a few iterations as time marching progresses. A typical run takes about 35 h on a Pentium-III 1 GHz PC. Additional details concerning the numerical approach can be obtained in Ref. 14.

Results

A total of 24 simulations was performed on various venturi orifices with throat diameters ranging from 0.1 to 2.9 in. and different shapes (the profile of the convergent section was either circular or conical in the devices modeled). Experimental flow-rate measurements were obtained on many of these devices by researchers at NASA Stennis Space Center and Pennsylvania State University. The fluids tested include cryogenic fluids (liquid oxygen, liquid nitrogen, and liquid hydrogen) and water. Computational results were compared with experimental results, which were available.

Table 1 shows all of the working conditions simulated. Cases 1–12 are for cryogenic fluids, and the calculations were undertaken by keeping inlet pressure as constant, 2150 psia, and varying outlet pressure, that is, the ratio of the pressure drop to the inlet pressure. Cases 12–24 are for water, and the calculations were performed by keeping outlet pressure as constant, namely the ambient pressure, and varying the inlet pressure.

Unsteady results were obtained in the very high Reynolds-number cases 1–12; the size of the cavitation region grew and collapsed in a quasi-periodic fashion in these cases. For those relatively low-Reynolds-number flows (cases 13–24) the effect of viscous terms and Reynolds-stress terms become more significant. These terms tend to smear out the unsteady oscillation in the cavitation extent. This is one of the tradeoffs in performing time averaging or mass averaging in turbulence modeling. Because we have chosen a time-averaging scheme, we lose some resolution of the unsteady effects for these low Reynolds-number cases. However, laminar solutions were computed on many of these cases, and unsteady results were predicted in these cases. Experimental evidence[15] indicates that flows of this type are inherently unsteady, even at fairly low Reynolds numbers (in the order of 10^3–10^4).

Figure 5 shows the typical contours of pseudodensity at different times during a typical cycle of bubble cavity growth. The vapor cloud always is anchored near the throat of the venturi and grows/shrinks in extent downstream of this point. In general, the growth portion of the cycle takes much longer than the collapse phase. In some cases the collapse caused a splitting of the cavity into two pieces. The collapse region is known to be subject to large gradients, and the computations show a sharp density gradient corresponding to this event. Experimental observations[4] also confirm this behavior.

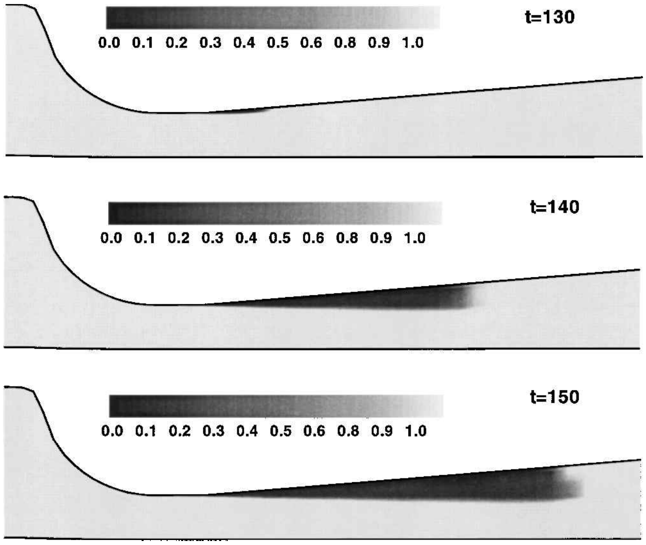

Fig. 5 Density contours, working fluid: liquid oxygen, $P_1 = 2150$ psia, and $P_2 = 1075$ psia (case 1 in Table 1).

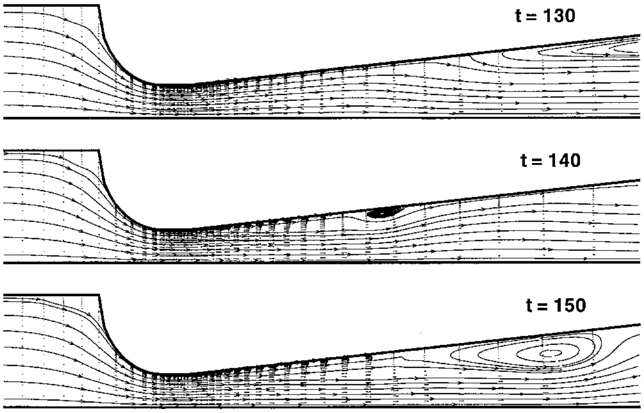

Fig. 6 Typical streamlines inside a venturi orifice, working fluid: liquid oxygen, $P_1 = 2150$ psia, and $P_2 = 1075$ psia (case 1 in Table 1).

Table 1 Summary of simulations conducted

Case	Fluid	D_t, in.	Re	K	$\bar{C}_D$	$L_C^{\max}/L_d$	St	$C_{D\,\mathrm{exp}}$
1	LOX	2.943	6.6×10^7	4.95	0.922	0.157	0.342	0.951*
2	LOX	2.943	6.6×10^7	3.30	0.915	0.213	0.295	0.951*
3	LOX	2.943	6.6×10^7	2.47	0.911	0.288	0.262	0.951*
4	LOX	2.943	6.6×10^7	1.98	0.913	0.338	0.232	0.951*
5	LN_2	2.943	9.7×10^7	4.80	0.921	0.149	0.344	0.960*
6	LN_2	2.943	9.7×10^7	3.20	0.916	0.223	0.296	0.960*
7	LN_2	2.943	9.7×10^7	2.40	0.925	0.300	0.260	0.960*
8	LN_2	2.943	9.7×10^7	1.92	0.919	0.387	0.229	0.960*
9	LH_2	2.508	3.6×10^8	4.77	0.931	0.133	0.374	——
10	LH_2	2.508	3.6×10^8	3.18	0.933	0.199	0.323	——
11	LH_2	2.508	3.6×10^8	2.39	0.938	0.269	0.291	——
12	LH_2	2.508	3.6×10^8	1.91	0.953	0.319	0.255	——
13	Water	0.100	1.9×10^5	1.051	0.849	1	——	0.831
14	Water	0.100	2.4×10^5	1.031	0.850	1	——	0.832
15	Water	0.100	2.9×10^5	1.021	0.850	1	——	0.833
16	Water	0.100	3.2×10^5	1.018	0.850	1	——	0.835
17	Water	0.125	3.3×10^5	1.027	0.853	1	——	0.884
18	Water	0.125	3.7×10^5	1.021	0.853	1	——	0.877
19	Water	0.125	4.0×10^5	1.018	0.853	1	——	0.878
20	Water	0.125	4.3×10^5	1.015	0.853	1	——	0.771
21	Water	0.208	2.1×10^5	3.704	0.911	0.188	——	——
22	Water	0.208	2.5×10^5	1.937	0.913	0.249	——	——
23	Water	0.208	2.9×10^5	1.566	0.914	0.361	——	——
24	Water	0.208	3.3×10^5	1.406	0.913	0.465	——	——

[a] * = measured at one backpressure. [b] —— = not available.

Figure 6 shows the streamlines at the same instants shown in Fig. 5. The physical domain extends downstream of the region depicted that is, the right-hand boundary on the plot is not the edge of the computational domain. As seen from the plots, the flow tends to separate near the aft end of the cavity. Numerous researchers have pointed to the violence of a cavity collapse as the local pressure rises rapidly leading to a local backflow region near the wall. Similar behavior has been noted in orifice flows[9] in prior work. At the end of of the cavitation region, circulation is generated as a result of bubble collapse.

Figure 7 shows nondimensional pressure contours at the instants corresponding to that in Fig. 5. In this plot dashed lines denote negative pressure values. The nondimensional vapor pressure of this case is −0.23. As seen from the plots, the lowest pressure (vapor pressure) starts at the throat and extends a substantial distance downstream. Hydrodynamic nonequilibrium effects inhibit the bulk of the liquid from vaporizing at this condition, and the vapor region is restricted to a small annulus near the wall as highlighted in Fig. 5. Note the sharp pressure rise near the collapse region in the $t = 140$ and 150 time slices. The pressure wave is highly unsteady and moves along the wall very rapidly as observed and studied in detail in cavitating

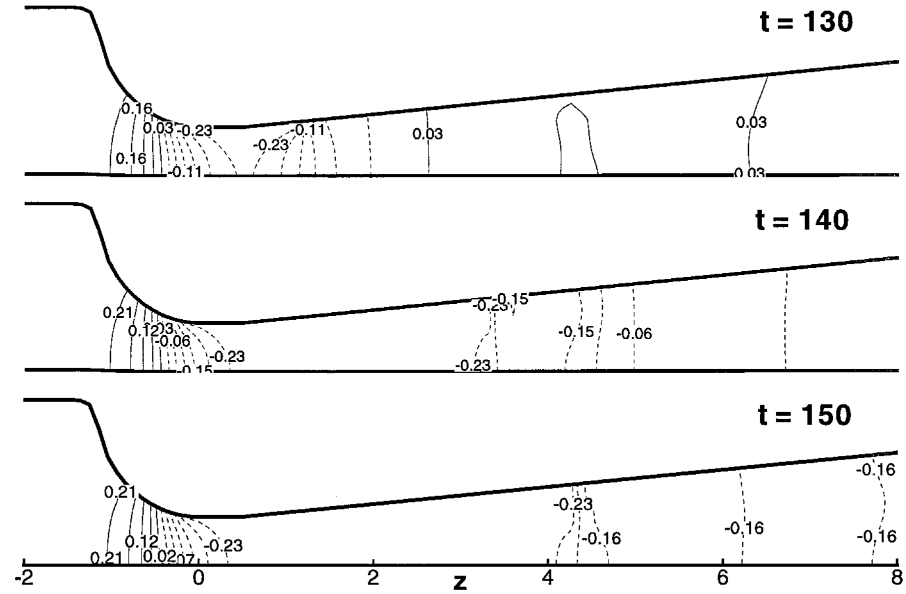

Fig. 7 Pressure contours, working fluid: liquid oxygen, $P_1 = 2150$ psia, and $P_2 = 1075$ psia (case 1 in Table 1).

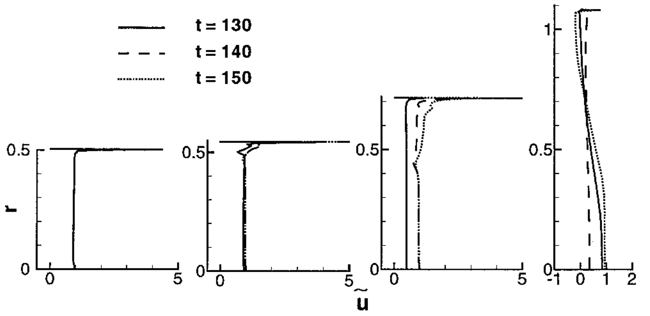

Fig. 8 Streamwise mean velocity profiles at $x = 0, 1, 3, 7$, working fluid: liquid oxygen, $P_1 = 2150$ psia, and $P_2 = 1075$ psia (case 1 in Table 1).

orifice flows.[9] Individual bubble collapses are not modeled in this homogeneous flow formulation.

The dimensionless streamwise mean velocity $\tilde{u}$ profiles at different axial locations $z = 0, 1, 3, 7$ at the same times depicted in Figs. 5–7 are shown in Fig. 8. The $z = 0$ data are at the throat, and downstream locations are depicted in the scale on Fig. 7. A strong positive pressure gradient is induced by the diffuser in the (see Fig. 7), causing the axial mean velocity near the wall at $z = 0, 1, 3$ to be much higher than that in the core region. The maximum velocity near the wall is nearly five times as the Bernoulli velocity computed by Eq. (4), indicating the two-dimensionality of the flow. In the diffusion section the flow is subject to an adverse pressure gradient and eventually separates from the wall in the aft part of the diffuser. Reverse flow is noted at all three time slices at the $z = 7$ location.

Figures 9 and 10 shows a typical history of discharge coefficient and cavitation length. Here, discharge coefficient is defined as the ratio of the computed mass flow rate to the theoretical mass flow rate based on Bernoulli velocity

$$\dot{m}_{\text{th}} = \rho_l A_t V_t \tag{16}$$

where A_t is the cross-section area at the throat. The computed mass flow rate is obtained by integrating the mass flux at either the throat or the exit plane. The location of the integration did not affect the mean C_D values, but did cause a phase shift in the plot. The cavitation length L_C is nondimensionalized using the throat diameter and is defined as the most downstream point where pseudodensity is equal to 0.98. The sharp density gradients in the collapse region make the L_C value insensitive to this threshold level.

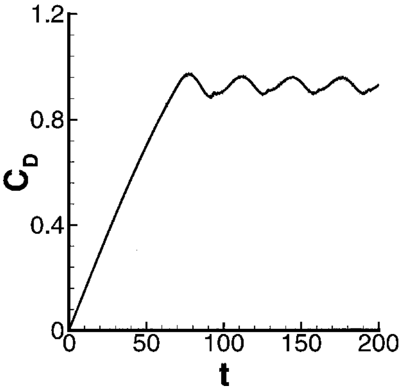

Fig. 9 Typical discharge coefficient history, working fluid: liquid hydrogen, $P_1 = 2150$ psia, and $P_2 = 1720$ psia (case 9 in Table 1).

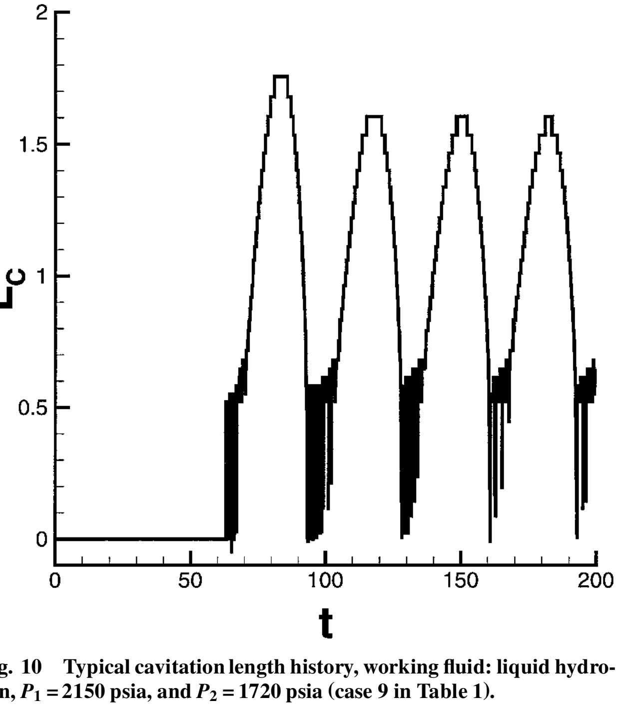

Fig. 10 Typical cavitation length history, working fluid: liquid hydrogen, $P_1 = 2150$ psia, and $P_2 = 1720$ psia (case 9 in Table 1).

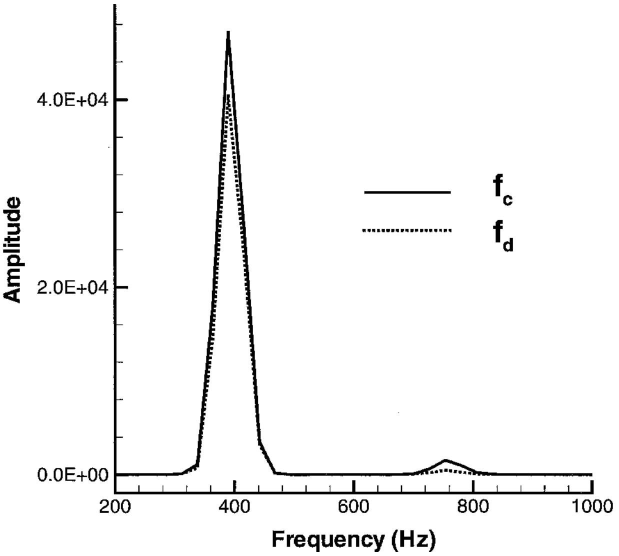

Fig. 11 Spectrum of cavitation length and discharge coefficient oscillations, f_c: cavitation length oscillation frequency, f_d discharge coefficient oscillation frequency (case 9 in Table 1).

The operating conditions of Figs. 9 and 10 correspond to case 9 in Table 1, where the working fluid is liquid hydrogen and the upstream pressure is held as 2150 psia and backpressure is held as 1720 psia. The linear rise in C_D and $L_C = 0$ region from $0 < t < 70$ are artifacts of the startup process as the assumed initial conditions at interior points are purged from the flowfield. The oscillations in flow and the cavity growth are tightly coupled. The maximum flow rate corresponds to the time when the cavity is near its largest value; the growth of the cavity acts to push fluid that is already in the diffuser out the exit. During the collapse phase, the opposite effect is present as liquid fills in the volume previously occupied by the vapor cloud. The oscillations are a high enough frequency that they would effect the accuracy of only the shortest tests, that is, long-duration tests go through so many oscillations that only the average C_D value is pertinent.

By performing Fourier transformation, we can obtain the principal frequency of oscillation of discharge coefficient and cavitation length. Figure 11 shows the spectrum for the results in Figs. 9 and 10. Results indicate that the bulk of the energy is contained at a single frequency; there is some response at the second harmonic of this primary tone. Note that the transforms for both mass flow and cavitation length show nearly identical frequency content because the extent of bubble cavity is the primary cause in the fluctuation of mass flow.

In testing of cryogenic propellants, it is often difficult to ensure a constant temperature venturi inflow condition due to stratification within the holding tank. For this reason the influence of inlet temperature was investigated for the liquid oxygen venturi used in cases 1–4 in Table 1. Because we have a hydrodynamic model and do not solve an energy equation, the sole influence of temperature changes is in the change in the fluid vapor pressure and hence the cavitation number K.

Figure 12 shows the discharge coefficient histories for three different liquid oxygen (LOX) inlet temperatures. For LOX temperatures of 80, 94, and 110 K, the associated vapor pressures are 4.4, 23.6, and 78.8 psia, respectively. As seen from the plot, variation of temperature (and the associated changes in vapor pressure) has very little effect on discharge coefficient. For all three temperatures the resultant average discharge coefficient is the same. The reason for this behavior is that the vapor pressures for the entire 80–110 K range are all relatively low in comparison to the inlet pressure of 2150 psia; for this reason all three cases have nearly identical cavitation index values.

As mentioned in the prior section, the nucleation site density $\hat{n}_o$ is an input parameter for the cavitation model used in the simulations. In principle, this property can be measured via microscopic evaluation of the fluid itself. Microparticles serve as nucleation sites, and it is widely known that "clean" fluids can tolerate and exhibit lower cavitition threhold pressures as a result of a limited number of sites. Unfortunately, it is very difficult to measure submicron sites that can actively support cavitation, and the influence of the wall (its structure and microchemistry) is also difficult to assess. For this reason, we undertook a study to investigate the sensitivity of results to this parameter. Previous studies in orifice flows[9] have shown that cavitation is not sensitive to this parameter when $\hat{n}_o > 10^8$ sites/m^3.

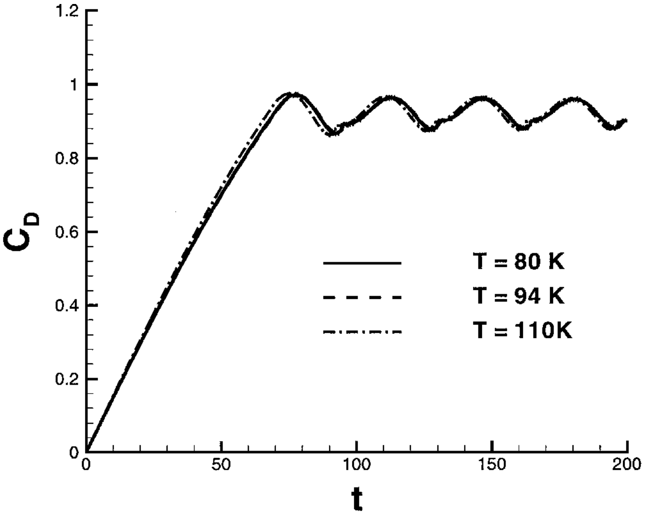

Fig. 12 Effect of temperature on discharge coefficient, working fluid: liquid oxygen, case 1, $T_{\rm in} = 94$ K, $P_1 = 2150$ psia, and $P_2 = 1720$ psia.

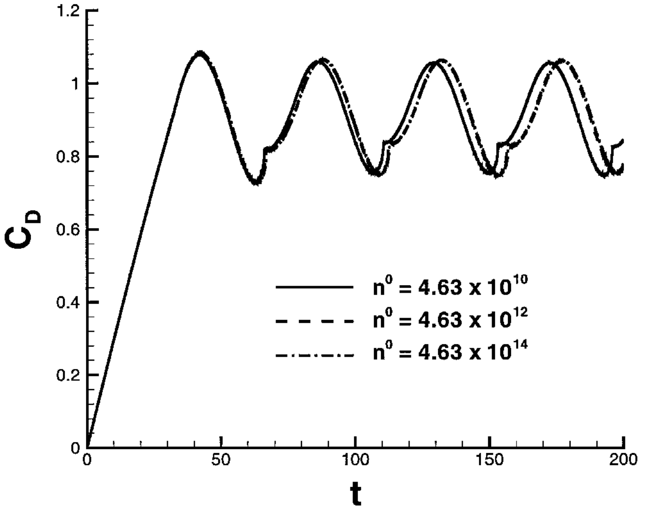

Fig. 13 Effect of site density on discharge coefficient, working fluid: liquid oxygen, case 4, $T_{\rm in} = 94$ K, $P_1 = 2150$ psia, and $P_2 = 1075$ psia.

Figure 13 depicts the results of $\hat{n}_o$ variations on the discharge. As seen from the plot, the average discharge coefficient changes little over a four-order-of-magnitude change in site density. For this reason, we decided to use the value of 4.63×10^{12} sites/m^3 for all simulations performed in this study. Here we note that this value has been used in prior orifice studies and lies within the range quoted by experimentalists as reasonable for most working fluids.

It was desirable to determine the influence of the fluid vapor pressure on the overall performance of the venturis studied. To assess this factor, the discharge coefficient and the maximum cavitation length during a cycle were time averaged over several periods of the oscillation once a limit-cycle behavior was obtained. These results, as well as the Strouhal number for the oscillation, are plotted as a function of cavitation number in Fig. 14. The average discharge coefficient is shown in the upper plot in Fig. 14. Although there is some scatter in the results, the discharge characteristics exhibit

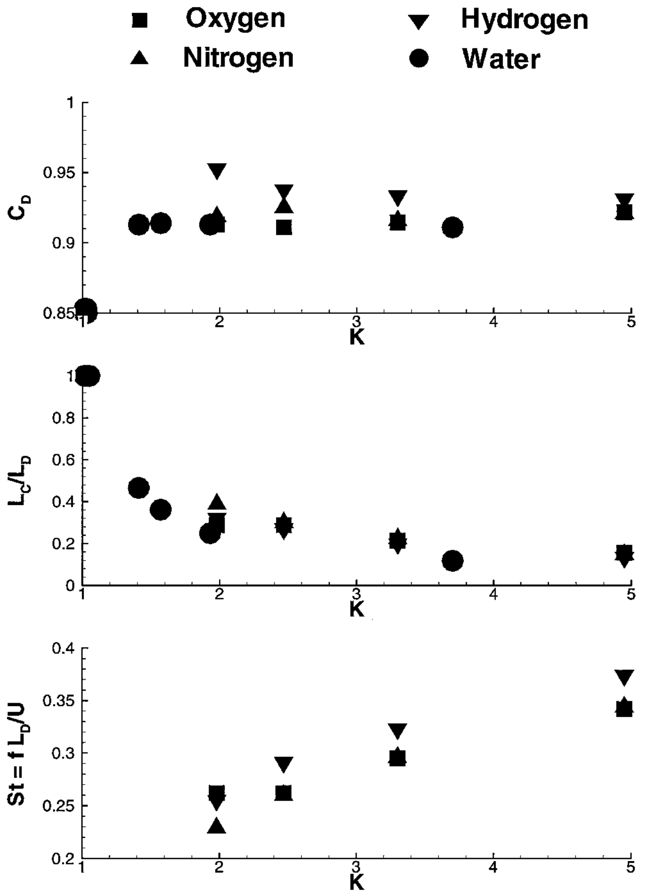

Fig. 14 Average discharge coefficient, average maximum cavitation length, and Strouhal number vs cavitation number.

no discernable trends with changing fluid vapor pressure. In most cases considered, the inlet pressures used were much greater than the vapor pressure. In practical devices this is almost always the case. The one case at $K \approx 1$ does show a significantly lower average discharge coefficient for this reason. We should also point out that the venturi geometry has a significant impact on C_D values and that the database in Fig. 14 contains venturis of differing designs.

The middle curve in Fig. 14 shows the variation of the maximum cavitation length, nondimensionalized against the length of the diffuser L_D, with cavitation number. Here, there is a strong dependence on the maximum size of the region with changes in K. When K is small, the downstream pressure is nearly equal to the fluid vapor pressure, and very large cavities result. In fact, in some cases the cavity can extend beyond the end of the diffuser. As K grows large, the maximum cavity length takes on an asymptotic behavior; for the practical values of K shown, there is still significant evidence of cavitation as maximum L_C/L_D values are still in the range of 10–15%. Here, we note that similar behavior has also been observed/computed in cavitating orifice/slot flows.[9,15]

The bottom curve in Fig. 14 depicts dimensionless oscillation frequencies (Strouhal numbers) for cases where quasi-periodic oscillations were obtained. The Strouhal number was defined using the diffuser length and Bernoulli velocity:

$$St = fL_D/V_t \tag{17}$$

Physically, this parameter represents the number of times the cavity oscillates during the time it takes a fluid element to traverse the diffuser at the Bernoulli velocity. The oscillation frequencies are in general inversely proportional to cavitation lengths. Similar results have been observed/computed in cavitating slot/orifice flows.[9,11,15] The Strouhal numbers obtained in this study are lower than those computed by Bunnell et al.[9] for a cavitating injector slot caused by the deceleration of the fluid in the diffuser in the present case.

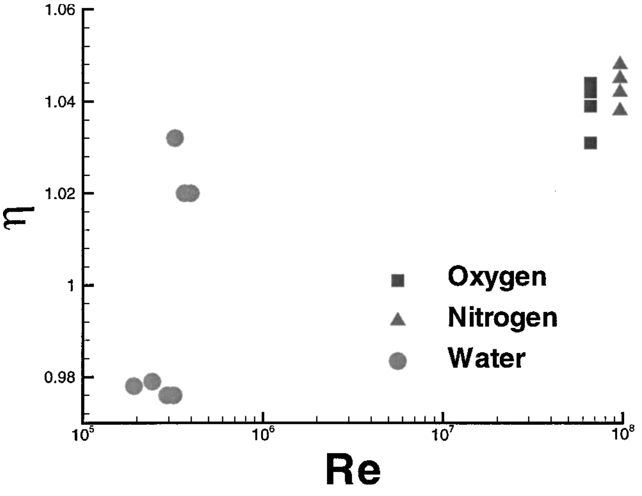

Fig. 15 Ratio of experimental/computed discharge coefficient vs Reynolds number.

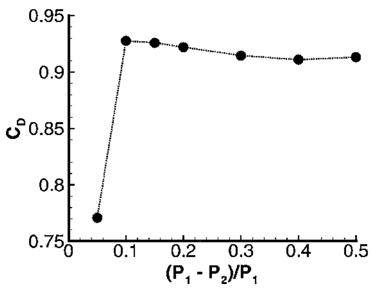

Fig. 16 Sensitivity of mass flow to downstream pressure, liquid oxygen venturi in cases 1–4 of Table 1.

Significant sound and vibration can be attributed to these oscillations as the cavitation collapse event can be quite violent. Because the oscillations of the bubble cavity and mass flow rate couple tightly with each other, this information is important to understand how the facility may affect engine stability in the case of rocket propulsion or other combustion devices. The venturi can be responsible for sending relatively high-amplitude tones into the combustion chamber.

The predictive capabilities of the model are summarized by comparing measured flow rates (where available, see Table 1) with computations. Figure 15 shows the variation of η vs cavitation number where η is simply the ratio of experimental-to-computed C_D values:

$$\eta = C_{D\exp}/\bar{C}_D \tag{18}$$

As shown from the plot, the model is capable of predicting the discharge coefficient within 2–5% compared with the experimental results. Similar accuracy has been noted in computations of orifice flows. Errors can be attributed to a variety of sources including deviations of the actual geometry with that modeled, turbulence effects from the inflow, and limitations regarding the assumptions of the model itself. In addition, the lack of an energy equation in the simulations could also account for some of the discrepancies. In general, there is a need to predict discharge characteristics much more accurately than 2–5%, and so additional model calibrations and improvements would be required to have a valuable predictive capability. In addition, at present we do not believe there are sufficient data to show any significant trends with the Reynolds number.

Finally, we wish to assess the sensitivity of the flow rate through the venturi to changes in backpressure. Cavitating venturis are believed to provide a flow rate that is insensitive to backpressure once the pressure is lowered to the point where cavitation occurs at the throat. Figure 16 shows the effect of variation of backpressure on average discharge coefficient for the liquid oxygen venturi studied in cases 1–4 in Table 1. As seen from the plot, the flow transits from unchoked mode to choked mode somewhere between 5 and 10% ΔP. Under choked conditions there is a slight variation in the average mass flow rate as backpressure changes. As the backpressure is lowered [$(P_1 - P_2)/P_1$ growing], the mass flow decreases by a few percent and actually reaches a minimum at $(P_1 - P_2)/P_1 = 0.4$; as the P_2 value is reduced further, the discharge actually increases. The explanation for this complex behavior is tied to the unsteady growth/collapse of the cavitation region and its effect on the average mass flow through the device. Similar deviations can be noted in the data for liquid nitrogen and hydrogen in Table 1. Because it is often desireable to have a venturi control of the flow rate to within 1%, this result indicates that the user must be alert to the effects of downstream pressure on the flow rate.

Conclusions

Two-phase flows through cavitating venturis have been studied with a homogeneous fluid approach using a $k - \omega$ turbulence model. A constitutive relation for the pseudodensity has been used to reflect the growth/collapse dynamics simulated in the Rayleigh–Plesset equation. Results indicate that the vapor cavity exists in a region near the wall downstream of the throat. The cavity oscillates in quasi-periodic fashion and does lead to unsteadiness in the mass flow produced by the device. The maximum size of the cavity is inversely proportional to the cavitation number, while the oscillation frequency increases with increasing cavitation number. In contrast to conventional belief, the venturi mass flow is a weak function of backpressure, even under cavitating flow conditions. Mass-flow variations of a 1–2% were demonstrated over a range of backpressures for a liquid oxygen venturi.

References

[1] Randall, L. N., "Rocket Applications of the Cavitating Venturi," *ARS Journal*, Vol. 22, No. 1, 1952, pp. 28–31.

[2] Judge, J. F., "Venturi Offer Test Stand Flexibility," *Missiles and Rockets*, Vol. 14, No. 8, 1964, pp. 28, 29.

[3] Fox, Z., "Cavitating Venturis and Sonic Nozzles," National Conference on Fluid Power, National Fluid Power Association, Oct. 1977.

[4] Sun, B.-H., and Yang, W. J., "Oscillatory Cavitating Flows in a Convergent-Divergent Nozzle," *Fluids Engineering Div. Publication FED*, Vol. 177, 1993, pp. 95–100.

[5] Ungar, E. K., Dzenitis, J. M., and Sifuentes, R. T., "Cavitating Venturi Performance at Low Inlet Subcooling: Normal Operation, Overflow and Recovery from Overflow," *Fluids Engineering Div. Publication FED*, Vol. 190, 1994, pp. 309–318.

[6] Ungar, E. K., and Mal, T. D., "Potential Cavitating Venturi Modifications to Improve Performance at Low Inlet Subcooling: Backward Facing Step and Threaded Throats," *Fluids Engineering Div. Publication FED*, Vol. 190, 1994, pp. 319–327.

[7] Navickas, J., and Chen, L. L., "Cavitating Venturi Performance Characteristics," *Fluids Engineering Div. Publication FED*, Vol. 177, 1993, pp. 153–159.

[8] Chen, Y., and Heister, S. D., "Modeling Hydrodynamic Non-Equilibrium in Bubbly and Cavitating Flows," *Journal of Fluids Engineering*, Vol. 118, No. 1, 1995, pp. 172–178.

[9] Bunnell, R. A., Heister, S. D., Yen, C., and Collicott, S. H., "Cavitating Injector Flows: Validation of Numerical Models and Simulations of Pressure Atomizers," *Atomization and Sprays*, Vol. 9, No. 5, 1999, pp. 445–465.

[10] Bunnell, R. A., and Heister, S. D., "Three-Dimensional Unsteady Simulation of Cavitating Flows in Injector Passages," *Journal of Fluids Engineering*, Vol. 122, No. 4, 2000, pp. 791–797.

[11] Xu, C., Bunnell, R., and Heister, S., "On the Influence of Internal Flow Structure on Performance of Plain-Orifice Atomizers," *Atomization and Sprays*, Vol. 11, No. 3, 2001, pp. 335–350.

[12] Kubota A., Kato, H., and Yamaguchi, H., "A New Modeling of Cavitating Flows: A Numerical Study of Unsteady Cavitation on a Hydrofoil Section," *Journal of Fluid Mechanics*, Vol. 240, 1992, pp. 59–96.

[13] Wilcox, D. C., *Turbulence Modeling for CFD*, 2nd ed., DCW Industries, La Canada, CA, 1998.

[14] Xu, C., "Simulation of Orifice Internal Flows Including Cavitation and Turbulence," Ph.D. Dissertation, School of Aero. and Astro., Purdue Univ., West Lafayette, IN, Dec. 2001.

[15] Chandra, B. W., and Collicott, S. H., "Experimental Investigation of Cavitation Frequency in a Slot Orifice," *ILASS- Americas'99, 12th Annual Conference on Liquid Atomization and Spray Systems*, 1999, pp. 379–384.